CrystEngComm

ROYAL SOCIETY OF CHEMISTRY

PAPER

View Article Online
View Journal | View Issue

Cite this: *CrystEngComm*, 2025, **27**, 6174

Surface sensitive catalytic mechanism of morphology and facet controlled α-MnO_2 nanostructures in the decomposition of ammonium perchlorate

Santra Merin Saju and Anuj A. Vargeese *

The catalytic properties of nanostructured materials are significantly influenced by their specific crystallographic facets. Each facet presents unique atomic configurations and electronic structures, which play a crucial role in bond activation, reactant adsorption, and the stabilization of intermediates. This study investigated the influence of distinct α-MnO_2 nanostructures on the thermal decomposition of ammonium perchlorate (AP), an important oxidizer in solid propellants. MnO_2 nanorods (1D) and nanocubes (3D) were synthesized and their catalytic activities were assessed. Nanocubes, featuring a microporous structure and predominantly exposing the (211) crystallographic facet, demonstrated enhanced catalytic efficiency in the decomposition of AP compared to nanorods primarily exposing the (310) facet. XPS analysis confirmed the presence of Mn^{4+}/Mn^{3+} redox couples and surface oxygen vacancies, which collectively facilitated electron transfer to the perchlorate anion (ClO_4^-), thereby promoting its reduction and accelerating one of the kinetically competing decomposition reactions. This resulted in a significant enhancement in NO_2 evolution relative to N_2O, during the decomposition reaction, suggesting a catalyst induced alteration in the decomposition pathway.

Received 22nd July 2025,
Accepted 25th August 2025

DOI: 10.1039/d5ce00732a

rsc.li/crystengcomm

Introduction

Understanding the relationship between morphology, surface structure, and surface properties is fundamental to materials development, as the physicochemical behaviour of a material is largely governed by the nature and orientation of its exposed crystallographic facets. This underscores the essential role of facet engineering in tailoring the material performance for applications in catalysis, sensing, and energy conversion,[1,2] where surface properties play a vital role. Among transition metal oxides (TMOs), manganese oxides, known for their multiple oxidation states, are of particular importance because of their broad applicability in catalysis, lithium-ion batteries, molecular sieves and water treatment.[3–7] Manganese dioxide (MnO_2) is a versatile material with wide ranging applications in catalysis,[8–10] ion separation[11] and as an electrode material in Li/MnO_2 batteries.[12] MnO_2 exists in multiple polymorphic forms, including tetragonal (α- and β-), orthorhombic (γ-), and hexagonal (ε- and δ-) crystal structures. Usually, the surface energy is intricately linked to the crystallographic orientation of the exposed facets.[13–16] During synthesis, nanoparticles typically assume morphologies that reduce the total surface energy, frequently resulting in configurations such as cubes, rods, or plates, which are determined by predominant exposed facets.[17] Altering the morphology and dimensions of the particles affects the physicochemical properties due to the changes in the arrangement and availability of the surface atoms.

Recent studies have explored the design of MnO_2 with engineered crystal facets and tuneable porosity, aiming to optimize its morphology and surface properties at both the micro- and nanoscale levels. Such materials include α-MnO_2 nanorods, nanospheres,[18–20] β-MnO_2 nanorods, nanotubes,[21–23] γ-MnO_2 nanowires,[24,25] δ-MnO_2 nanosheets[21] and nanoflakes.[26,27] Among these, α-MnO_2 has attracted particular interest owing to its tuneable surface properties and outstanding catalytic and supercapacitor performances. Fig. 1 shows the crystal structure of α-MnO_2 generated using the Vesta 3 software.[28] α-MnO_2 is composed of Mn^{4+} ions and highly polarizable O^{2-} ions, arranged in a framework of corner- and edge-sharing MnO_6 octahedra. Its crystal structure features (1 × 1) and (2 × 2) tunnel-like channels formed by double chains of edge-sharing MnO_6 octahedra, which contribute to its intercalation capability and ion

Laboratory for Energetic and Energy Materials Research (LEEMR), Department of Chemistry, National Institute of Technology Calicut, Kozhikode 673601, India. E-mail: aav@nitc.ac.in

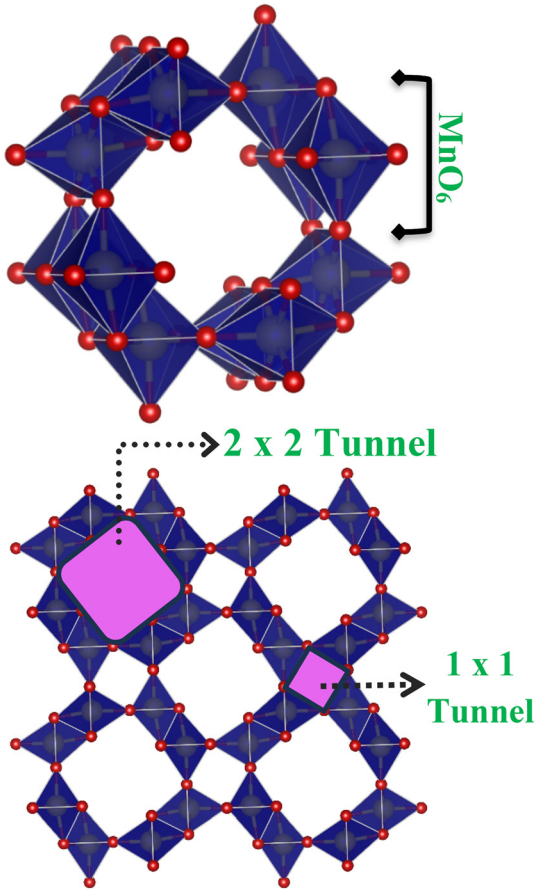

Fig. 1 Crystal structure of α-MnO_2. Small (red) spheres are oxygen and large (yellow) manganese lie inside the indicated approximate MnO_6 octahedra forming the (2 × 2) and (1 × 1) tunnels.

transport properties, making it suitable for catalytic and energy storage applications.

Considering that all heterogeneous catalytic reactions occur at the catalyst surface, an attempt was made to establish an intrinsic relationship between the well-defined chemical and structural characteristics of nanoparticles and their catalytic behaviour. In this study, two morphologically distinct MnO_2 nanostructures – nanorods and nanocubes – were synthesized. To elucidate the structural characteristics of MnO_2, the exposed facets were identified using various diffraction techniques and transmission electron microscopy. Furthermore, the influence of α-MnO_2 nanorods and nanocubes, along with their respective surface structures on the thermal decomposition mechanism of ammonium perchlorate (AP) was examined through evolved gas analysis.

Experimental

Materials

Manganese nitrate tetrahydrate ($Mn(NO_3)_2{\cdot}4H_2O$) was procured from Sigma-Aldrich, and sodium bicarbonate ($NaHCO_3$) was obtained from Merck Life Science Pvt. Ltd. Potassium permanganate ($KMnO_4$) was sourced from Nice Chemicals Pvt. Ltd., and manganese sulphate monohydrate ($MnSO_4{\cdot}H_2O$) was acquired from Fischer Scientific Pvt. Ltd. All reagents were used as received, without any additional purification. Ammonium perchlorate (AP) with an average particle size of 35 μm was prepared by the reaction between perchloric acid and ammonia solution.

Synthesis of MnO_2 nanorods and nanocubes

MnO_2 nanorods (MnR) were synthesized using a hydrothermal method.[29] In a typical procedure, 0.50 g $KMnO_4$ and 0.21 g $MnSO_4{\cdot}H_2O$ were individually dissolved in deionized water (15 mL). After complete dissolution, both the solutions were combined and magnetically stirred for 20 min to ensure homogeneity. The resulting mixture was then transferred to a Teflon-lined stainless-steel autoclave and subjected to hydrothermal treatment at 160 °C for 12 h. Following the reaction, the solid product was recovered by centrifugation, dried in a hot air oven at 80 °C overnight, and calcinated at 400 °C for 2 h.

A precipitation method[30] was optimized for the synthesis of MnO_2 nanocubes (referred to as MnC). 100 mL aqueous solution of manganese nitrate tetrahydrate (0.1 M) in distilled water was prepared in a three-necked round-bottom flask and the solution was slowly heated to 90 °C. Once the target temperature was achieved, the pH of the solution was gradually increased to 9 through the controlled addition of $NaHCO_3$ at a rate of 25 mL h^{-1}, using a syringe pump, under continuous stirring. The reaction mixture was kept under these conditions for 3 h, cooled to room temperature and stirred overnight to guarantee complete precipitation. The obtained solid product was separated through decantation, thoroughly washed with distilled water, and separated *via* centrifugation. The precipitate was dried at 70 °C overnight in hot air oven and later calcinated in two stages, first at 160 °C for 12 h, followed by 400 °C for another 12 h, resulting in the final product.

Characterization of MnO_2 nanorods and nanocubes

Powder X-ray diffraction (P-XRD) analysis of the prepared samples was conducted at ambient temperature (25 °C) using a PANalytical X'Pert^3 Powder X-ray diffractometer equipped with a Cu Kα radiation source (λ = 1.54 Å). The diffraction patterns were recorded over a 2θ range of 20–70°, with a step size of 0.0263°. The obtained diffraction patterns were analysed using X'Pert HighScore Plus software and compared with standard reference patterns from the International Centre for Diffraction Data (ICDD) database for phase identification. The morphological and surface characteristics of the synthesized MnO_2 samples were examined using a ZEISS Sigma 300 scanning electron microscope (SEM). For SEM analysis, the ground powder sample was dispersed in a volatile solvent, ultrasonicated, and subsequently drop-cast onto a clean glass slide. After drying, SEM images were recorded. SEM images were used to investigate the particle size, shape, surface texture, and porosity. The average particle

size was estimated using ImageJ software based on the SEM images.

Transmission electron microscopy (TEM) analysis was performed using JEOL JEM-F200 microscope operated at an accelerating voltage of 200 kV to provide further insight into the microstructural details of the MnO_2 particles. Gatan Digital Microscopy Suite software was used to analyse the selected area electron diffraction (SAED) patterns. The specific surface areas of the MnO_2 samples were evaluated using the Brunauer–Emmett–Teller (BET) method on a Belsorp-max instrument (MicrotracBEL Corp.). The chemical states of manganese and surface oxygen vacancies of the catalyst were analysed using X-ray photoelectron spectroscopy (XPS) on a Shimadzu Axis Supra+ instrument, equipped with a microfocused monochromatic Al Kα radiation source ($h\nu$ = 1486.6 eV). The C 1s peak (284.8 eV) was employed as the internal standard for calibration, and peak deconvolution was carried out using the XPSPeak41 software.

Preparation of AP–MnO_2 mixtures

Mechanical mixing was employed to prepare AP–MnO_2 mixtures containing 1% and 4% (by weight) MnR and MnC. The thermal characteristics and catalytic efficiencies of the resulting mixtures were examined.

Thermal analysis

The thermal decomposition of the AP and AP–MnO_2 mixtures was carried out using a PerkinElmer STA 6000 simultaneous thermal analyser under a nitrogen atmosphere. For the thermogravimetric-differential thermal analysis (TG-DTA) of AP–MnO_2 mixtures, approximately 1.2 mg of the sample was weighed and placed in a 100 μL open alumina crucible, followed by heating at 10 °C min^{-1} from room temperature to 500 °C. The recorded thermograms were analysed to evaluate the influence of MnO_2 nanostructures with different morphologies and exposed facets on the thermal decomposition of AP.

Thermogravimetric-Fourier-transform infrared spectroscopy (TG-FTIR) evolved gas analysis

The TG-FTIR evolved gas analysis was carried out using a Netzsch 209 F1 Libra TGA system coupled with a TG-FTIR interface connected to a Bruker Vertex 80 FTIR spectrometer. The thermogravimetric measurements were performed at a heating rate of 15 °C min^{-1}. The temperatures of the transfer line and IR gas cell were maintained at 210 °C and 190 °C, respectively. FTIR spectra were recorded in the range 650–3600 cm^{-1} with a resolution of 4 cm^{-1}.

Results and discussion

Characterization of catalyst

In the powder X-ray diffraction (P-XRD) patterns (Fig. 2a) of the synthesized MnO_2 samples, MnR and MnC, the diffraction peaks corresponded to the α-phase of MnO_2 (ICDD card no. 00-044-0141) with the tetragonal crystal structure (lattice constants: $a = b = 9.78$ Å and $c = 2.86$ Å; $\alpha = \beta = \gamma = 90°$). The most intense peak at $2\theta = 37.5°$ is assigned to the (211) plane, with other notable peaks appearing at 28.8°, 41.9°, 49.9°, 56.4°, 60.3°, and 65.1° corresponding to the (310), (301), (411), (600), (521) and (002) planes respectively, confirming the formation of a single-phase α-MnO_2 particles. MnR exhibited sharp, intense and well-defined peaks, indicating a highly crystalline nature, whereas, MnC showed broader low-intensity peaks, indicating a porous nature leading to a low degree of crystallinity and increased lattice strain relative to the nanorods. The

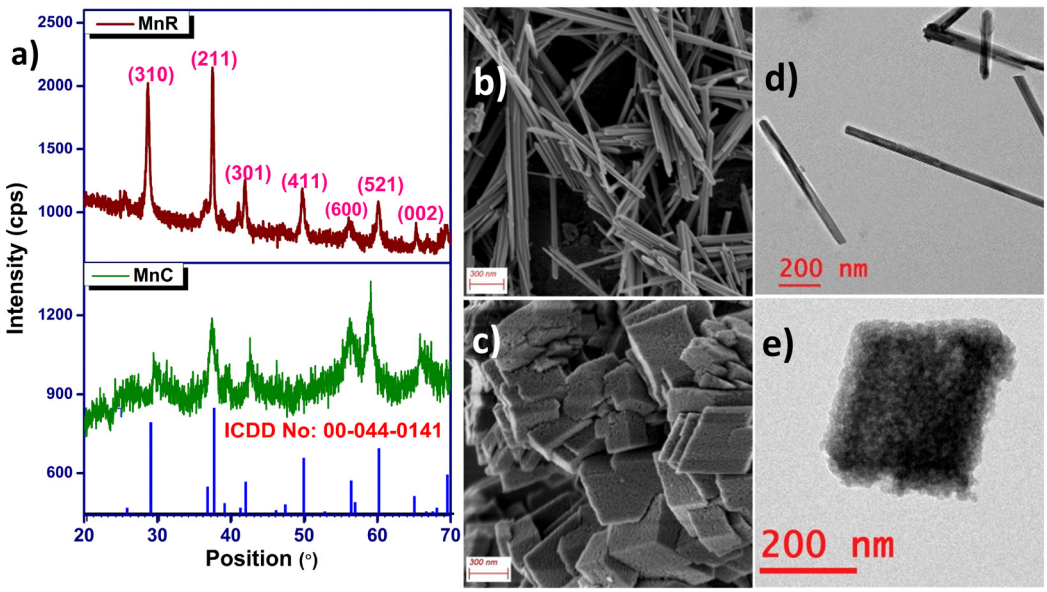

Fig. 2 (a) P-XRD pattern of MnR and MnC, (b and d) SEM and TEM images of MnR and (c and e) SEM and TEM images of MnC respectively.

Table 1 Surface area, total pore volume and average pore diameter determined by BET analysis of MnR and MnC

Sample	Surface area ($m^2\ g^{-1}$)	Total pore volume ($cm^3\ g^{-1}$)	Mean pore diameter (nm)
MnR	34.65	0.0229	1.32
MnC	60.81	0.0366	1.20

introduction of pores disturbed the periodic atomic arrangement, thereby reducing the number of coherently scattering atoms and leading to a reduction in the intensity of the X-ray diffraction peaks. Additionally, lattice defects and internal strain induced by pores within the crystal structure contributed to the peak broadening. Further, a significant difference in the preferred orientation was noted, with MnC exhibiting a low intensity ratio of the (310) plane to (211) plane, indicating predominant exposure of the (211) facet.

The SEM images (Fig. 2b, c, S1 and S2) show the morphologies of the synthesized MnO_2 samples. The MnO_2 sample synthesized *via* the hydrothermal method exhibited a rod-like morphology (Fig. 2b), with an average breadth of 85 nm and a length of 1050 nm (1.05 μm). The sample obtained using the precipitation method exhibited a porous cuboidal morphology (Fig. 2c) with an average particle size of 335 nm. The nanorod and nanocube morphologies of MnR and MnC are shown in their respective TEM images (Fig. 2d, e, S3 and S4). The aspect ratio (length to breadth ratio) of MnR and MnC were found to be 19.06 and 1.01 nm respectively, indicating that the bigger aspect ratio is conforming to the elongated shape of the MnR.

The surface areas and porosities of the synthesized MnO_2 samples were characterized using Brunauer–Emmett–Teller (BET) analysis. Table 1 summarizes the specific surface area, total pore volumes, and average pore diameters of MnR and MnC. The BET findings confirmed that the samples exhibited pore size characteristics of microporous materials (<2 nm). The specific surface areas of MnR and MnC were determined to be 34.65 $m^2\ g^{-1}$ and 60.81 $m^2\ g^{-1}$ respectively indicating that MnC possessed a larger surface area than the MnR.

XPS is a powerful tool for investigating the surface composition and electronic states of materials in the catalyst. The survey scan spectra (Fig. S5) and high-resolution Mn 2p spectra of MnR and MnC (Fig. 3a) display two prominent spin–orbit doublets centred at approximately 642 and 653 eV, corresponding to Mn $2p_{3/2}$ and Mn $2p_{1/2}$, respectively. Upon deconvolution, the Mn 2p spectrum revealed four distinct peaks corresponding to Mn^{3+} and Mn^{4+}. Peaks at ~642.1 eV and ~653.6 eV of MnR are assigned to Mn^{3+}, while the peaks at ~644.5 eV and ~655.1 eV are attributed to Mn^{4+}. Similarly, in the case of MnC, Mn^{3+} peaks were centred at 641.7 eV and 653.1 eV and Mn^{4+} peaks were centred at 644.1 eV and 654.9 eV. The XPS O 1s spectra of MnR and MnC (Fig. 3b) were analysed to examine the types of surface oxygen species and the presence of oxygen vacancies, which are closely linked to catalytic performance. Three distinct oxygen species were identified at binding energies of 529.5 eV (O_I), 530.7 eV (O_{II}), and 532.1 eV (O_{III}) in the case of MnR and at 529.1 eV (O_I), 530.8 eV (O_{II}), and 532.3 eV (O_{III}) for MnC, corresponding to lattice oxygen (O_I), chemisorbed oxygen or surface hydroxyls

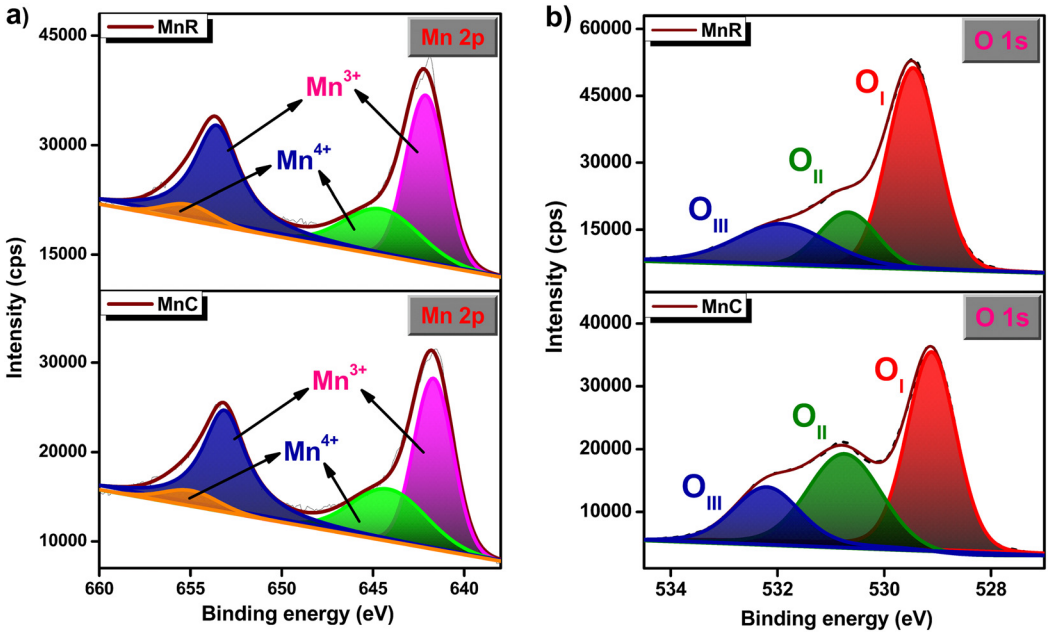

Fig. 3 High-resolution XPS a) Mn 2p spectra and b) O 1s spectra of MnR and MnC.

(O_{II}), and physisorbed water molecules (O_{III}), respectively. The O_I peak attributed to lattice oxygen, indicated the presence of Mn–O bonds. The O_{II} peak corresponds to hydroxyl groups or low-coordinated oxygen species (O^-, O_2^{2-}), which are typically associated with defect sites, thereby confirming the presence of oxygen vacancies. The enhanced intensity of the O_{II} peak in the MnC indicates an increased concentration of surface oxygen vacancies.[31]

Catalytic activity evaluation

AP is a widely used oxidizer in solid rocket propellants.[32,33] The efficiency of these propellants is closely linked to the decomposition behaviour of AP. Thermal analysis confirmed three key thermal events in the 200 to 400 °C region. As illustrated in Fig. 4, the initial event was an endothermic peak near 246 °C, corresponding to the phase transition from an orthorhombic to a cubic phase. This was followed by an exothermic low-temperature decomposition (LTD) event, characterized by the dissociative sublimation of AP, which released ammonia (NH_3) and perchloric acid ($HClO_4$). The NH_3 is adsorbed onto the newly formed surface pores of AP, thereby inhibiting its decomposition and consequently reducing the overall decomposition rate. Subsequently, a second exothermic high-temperature decomposition (HTD) event occurred, involving the decomposition of remaining undecomposed AP and the oxidation of the adsorbed products.[34]

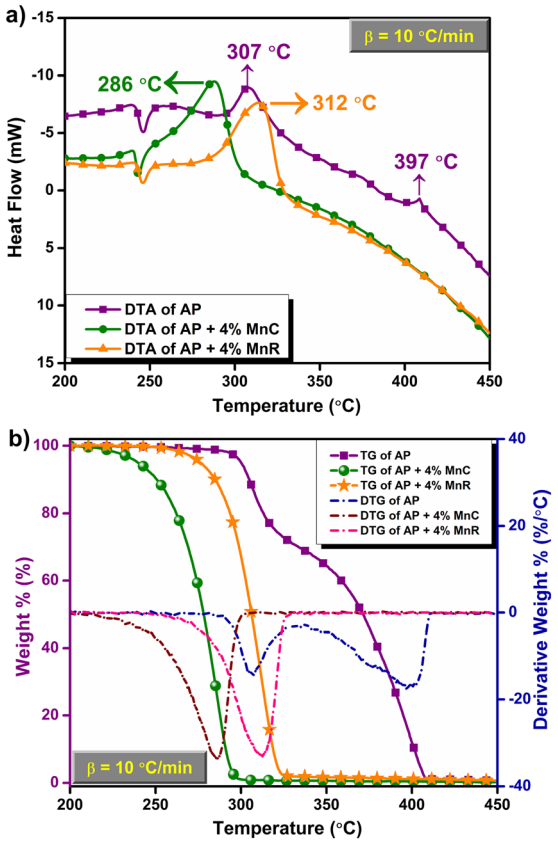

Fig. 4 a) DTA plot and b) TG-DTG plot of AP and AP + 4% MnR and MnC.

To study the catalytic effect of MnO_2 samples on AP, thermogravimetric analysis of AP–MnO_2 mixtures was performed. Fig. S6 shows the thermal analysis (TG-DTA) results for pure AP and AP mixed with 1% MnR and MnC. The addition of 1% MnR reduced the LTD peak temperature from 307 °C to 302 °C and the HTD peak temperature from 397 °C to 341 °C. A more significant reduction in decomposition temperature was observed with the addition of 1% MnC. The LTD and HTD peaks merged into a single exothermic event and the peak temperature was reduced to 305 °C, even below the LTD temperature of AP, which marks a reduction of 92 °C. This observation suggests that the incorporation of 1% MnC transforms the typical two-step thermal decomposition of AP into a single exothermic event which is a notable deviation from the typical decomposition behavior.[35] The catalytic effect and transformation were further validated using differential thermogravimetric (DTG) curves (Fig. S6b). Among the samples, MnC exhibited the most pronounced DTG peak, indicating the highest rate of mass loss ($\Delta m/\Delta T$) and reflecting its superior catalytic efficiency.

The thermal decomposition behaviour of AP is influenced by several parameters, including the particle size, surface area, morphology and amount of catalyst used.[4] In this study, the impact of varying MnO_2 concentrations on the decomposition profile of AP was also assessed. TG-DTA plots illustrating pure AP and AP with an increased weight percentage of MnO_2 are presented in Fig. 4. Notably, with the 4% addition of MnR and MnC, a significant decrease in the HTD peak temperature of AP was observed. The HTD peak temperature was reduced to 312 °C and 286 °C from 397 °C when AP mixed with 4% MnR and MnC respectively, indicating a substantial reduction in decomposition temperature with a difference of 111 °C. The variation of HTD peak temperature with varying concentrations of MnR and MnC is summarised in Fig. S7 and the LTD and HTD peaks merge into a single exothermic peak when 4% catalysts were mixed with AP. Lowering of HTD peak temperature with varying particle size and surface area of 4% MnO_2 samples is summarised in Fig. S8.

To elucidate the mechanistic variations in the catalytic decomposition of AP, TG-FTIR (Fig. S9–S11) evolved gas analysis was employed to monitor the evolution of the gaseous products. It is well established that the thermal decomposition of AP proceeds *via* multiple pathways,[36–38] yielding a complex mixture of gaseous species. Previous studies have identified NH_3, H_2O, HCl, $HClO_4$, NO_2, and N_2O as the primary decomposition products.[34,38,39] Below 300 °C, the thermal decomposition of AP predominantly followed a stoichiometric pathway represented by reaction R1. In contrast, at temperatures exceeding 380 °C, the decomposition enters an exothermic regime, characterized by a reaction mechanism described by reaction R2.[40] However, these stable species result from the secondary reactions. In

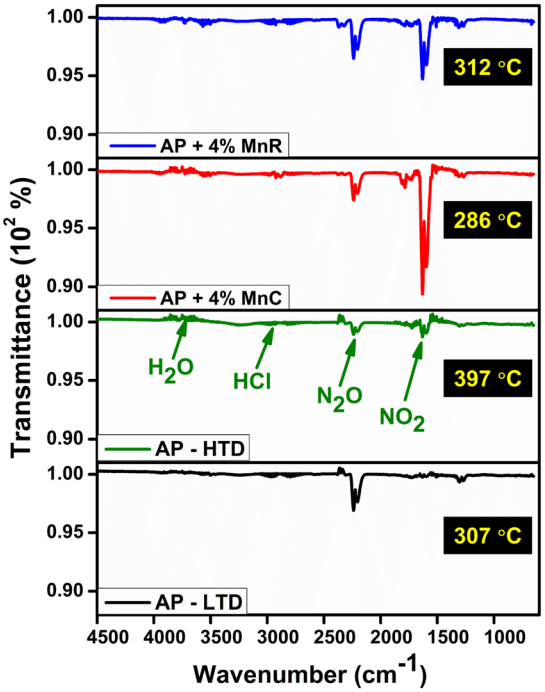

Fig. 5 Comparison of FTIR spectra of AP, AP–MnR and AP–MnC at peak decomposition temperature.

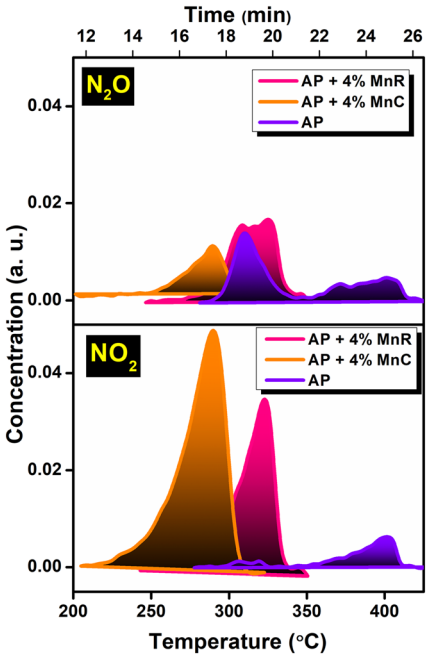

Fig. 6 Concentration profile of temporal and thermal evolution of N_2O and NO_2.

the present investigation, gaseous species evolved at the peak decomposition temperatures (LTD & HTD) were (Fig. 5) H_2O, HCl, N_2O, and NO_2. The incorporation of MnC and MnR resulted in a marked change in the concentration profiles of the evolved gases, suggesting a significant catalytic effect on the underlying decomposition mechanism. The temporal and thermal evolutions of N_2O and NO_2 concentrations are presented in Fig. 6.

$$4NH_4ClO_4 \rightarrow 2N_2O + 2Cl_2 + 8H_2O + 3O_2 \quad (R1)$$

$$2NH_4ClO_4 \rightarrow 2NO + Cl_2 + 4H_2O + O_2 \quad (R2)$$

In the absence of a catalyst, the relative concentrations of N_2O and NO_2 vary between the LTD and HTD stages, consistent with earlier reports[38] suggesting a competitive relationship between their formation pathways. However, in the presence of the catalyst, a marked increase in the NO_2 concentration relative to N_2O was detected, indicating a significant shift in the decomposition mechanism. This suggests that these catalysts promote pathways favouring the formation of NO_2 over N_2O, potentially altering the redox balance and AP decomposition kinetics. To understand the relative concentration change, the ratios of absorption values of N_2O to NO_2 for AP, AP–MnR, and AP–MnC were calculated (Table S1). The data indicate an increase in NO_2 concentration with respect to N_2O with the addition of the catalysts (AP < AP–MnR < AP–MnC), and the highest catalytic activity of MnC is also evident. When catalysed by MnO_2, the ability of manganese ions to cycle between multiple valence states (Mn^{4+}/Mn^{3+}) initially promotes faster electron transfer from perchlorate ions to ammonium ions. The MnO_2 surface further facilitated the adsorption of NH_3 and $HClO_4$ on its surface and mitigated the accumulation of the decomposed products on the surface of AP, thereby accelerating the decomposition of partially decomposed AP. AP does not achieve complete decomposition during the LTD stage, and NH_3 tends to adsorb onto its surface. However, MnO_2 will significantly reduce this adsorption over AP because of the preferential adsorption of NH_3 on the catalyst surface. Particularly in MnC, the porous nature advances the adsorption of LTD decomposed products onto the pores and eventually get reduced at high temperatures. The reduced surface area and porosity of nanorods compared to cuboidal morphologies limit the mass transfer and accessibility to active sites.

Previous studies employing thermal analysis techniques, TG-FTIR, TG-MS, and computational modelling have proposed a proton transfer mechanism governing the initial stages of AP decomposition. This mechanism involves the formation of key reaction intermediates as represented in reactions R3 to R9, where R7 and R8 occurring during the LTD stage and R9 during the HTD stage. This also shows the reactions leading to the formation of NO_2 and N_2O during different stages of decomposition.

Structure–property relationship

The morphology of MnO_2 nanostructures is significantly influenced by the synthesis method and the environment in which crystal growth occurs.[17] By fine-tuning these parameters, the morphology and particle size of the catalyst

is precisely controlled for targeted application. Controlled temperature methods allow for gradual crystal growth, supporting the development of faceted and well-ordered morphologies. Thus, the growth of elongated nanorods was promoted by the hydrothermal method when treated at 160 °C. High supersaturation promotes rapid nucleation, resulting in smaller less defined crystals. Hence, the precipitation method was adopted for the growth of nanocubes. In addition, the presence of $NaHCO_3$ changed the equilibrium saturation concentration and led to supersaturation, which encouraged rapid nucleation. In such an environment, the crystals grew equally along multiple directions, leading to the formation of nanocubes.

$$NH_4^+ClO_4^- \rightleftharpoons NH_3\text{–}H\text{–}ClO_4 \rightleftharpoons NH_3\text{–}HClO_4 \rightarrow NH_3 + HClO_4 \quad (R3)$$

$$HClO_4 + ClO_3^- \rightarrow ClO_4^- + HClO_3 \quad (R4)$$

$$HClO_3 \rightarrow ClO_2 + OH \quad (R5)$$

$$HClO_4 \rightarrow ClO_2 + HO_2 \quad (R6)$$

$$2ClO_2 + 2NH_3 \rightarrow N_2O + Cl_2 + 3H_2O \quad (R7)$$

$$ClO_2 + NH_4^+ \rightarrow N_2O + H_2 + HCl + H^+ \quad (R8)$$

$$ClO_2 + NH_3 \rightarrow H_2 + NO_2 + HCl \quad (R9)$$

To gain a deeper insight into the distinct catalytic behaviours of MnR and MnC during AP decomposition, their crystallographic characteristics were examined using high-resolution TEM (HR-TEM) and SAED. High magnification TEM images of MnR and MnC are shown in Fig. 7a and b respectively. Fig. 7c presents the SAED pattern, consisting of well-defined spots indicating the highly crystalline nature of MnR. The low crystallinity owing to the porous nature of MnC is demonstrated by the hazy spots in the SAED pattern presented in Fig. 7d. SAED patterns also offer crystallographic insights and are sensitive to the nanostructure and orientation of particles. Sharp SAED spots, as seen for MnR, when correlated with the P-XRD pattern, typically align with intense and narrow P-XRD peaks, indicating the high crystallinity of MnR. In contrast, hazy SAED spots typically appear as broadened and less intense P-XRD peaks, which is indicative of the reduced crystallinity and porous nature of MnC.

In heterogeneous catalysis with solid catalysts, catalytic activity occurs exclusively at the surface, making the surface structure and composition vital factors in determining performance. The simulated calculation result determined using the Gatan Digital Microscopy Suite software for lattice spacing is different for the two morphologies, indicating that MnR and MnC exhibit two different exposed surface planes. The interplanar spacing was determined from the FFT image derived from the marked area in the HRTEM image of the MnR as shown in Fig. 7e. The spot corresponds to the (310) plane with an interplanar spacing of 1.24 nm, which aligns

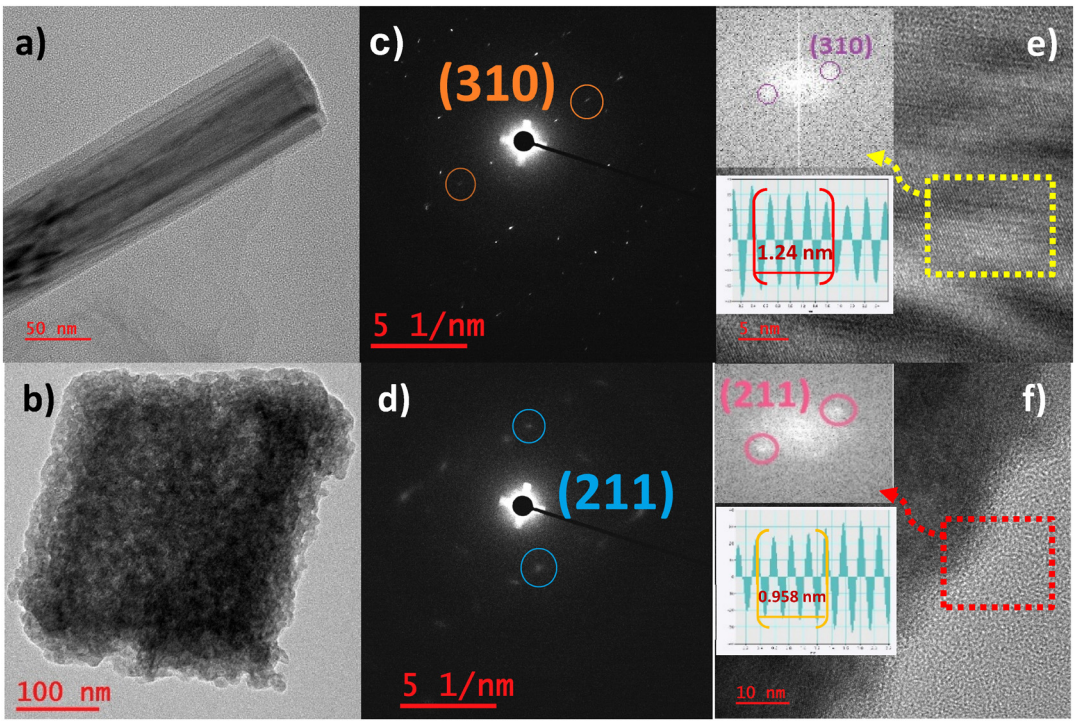

Fig. 7 TEM image of a) MnR and b) MnC; SAED pattern marked with the exposed surface c) MnR and d) MnC; HRTEM image with FFT image and simulated calculation result of lattice spacing as insets of e) MnR and f) MnC.

well with the peak observed at an angle of 28.8° in the ICDD card no. 00-044-0141. The interplanar spacing of 0.96 nm resulting from MnC (Fig. 7f), is associated with reflections from the (211) plane, which corresponds to the most intense peak at 2θ = 37.5°. This confirms that the surface composition of MnO_2 is mainly influenced by the specific exposed crystallographic planes. The exposed crystal planes present different atomic configuration and adsorption capabilities significantly influencing the catalytic performance. It was inferred from the TEM and SAED analyses that MnC primarily exposed the (211) crystal plane, whereas MnR displayed the (310) plane. These observations confirmed that the cuboidal morphology exposed high-index faceted (211) surfaces with high atom density, as illustrated in Fig. 8.

Earlier crystallographic studies have shown that MnO_2 with various morphologies exhibits unique crystal facets, each with distinct surface energies and stabilities. An earlier study[41] reported the surface energies of α-MnO_2, based on DFT calculations using PBE + U (Perdew–Burke–Ernzerhof with Hubbard U correction) method, and revealed that the low-indexed facets with the lowest energies are more stable. In that study, the surface energies of the high-indexed facets corresponding to those exposed by MnC and MnR in our work followed the sequence, (211) < (310), with reported values of 1.08 and 1.41 J m^{-2}. These disparities affect the energy necessary for the creation of oxygen vacancies, where a greater concentration of oxygen vacancies signifies reduced formation energy and high performing catalysts.[42]

Variations in exposed surfaces influence catalytic performance, as atomic configurations and surface energies of these facets govern interactions with AP decomposition intermediates. Typically, low-energy surfaces of MnO_2 crystals exhibit a higher concentration of oxygen vacancies, which promote enhanced catalytic activity and are more accessible than high-energy surfaces.[25] Oxygen vacancies within the catalyst are crucial in enhancing decomposition rate by acting as active sites. The presence of oxygen vacancies in MnO_2 samples, confirmed by XPS, and high intensity of Mn^{3+} peaks in MnR and MnC, indicate oxygen vacancies in both samples, which benefits catalytic activity. Among these samples, the O_{II}/O_I intensity ratio, reflecting relative concentration of oxygen vacancies, decreases in order of MnC (38.9%) > MnR (22.7%), suggesting MnC has the highest density of oxygen vacancies. The higher concentration of oxygen vacancies in MnC, confirmed by the spectral signatures, enhances catalytic performance by increasing surface reactivity and promoting ClO_4^- adsorption on nanocubes more effectively than on the AP surface.

The ClO_4^- generated from $HClO_4$ is a kinetically stable and strong oxidizer, but Mn^{4+}/Mn^{3+} surfaces catalyse its reduction to ClO_2. Moreover, the surface oxygen vacancies promote electron transfer to ClO_4^- further catalysing this reaction. This leads to the higher availability of ClO_2. NH_3 usually remain adsorbed onto the undecomposed AP, and the intimately mixed manganese-based catalyst would make the surface reduced ClO_2 readily available for reacting with the adsorbed NH_3, giving precedence to reaction R9. Hence, the concentration difference of NO_2 and N_2O in the presence of MnC and MnR, is attributed to the competing reaction between the reaction intermediates ClO_2 and NH_3 on the catalyst surface as described in reactions R7 and R9. Thus, the oxygen vacancies generated on the exposed (211) surface of MnC, markedly improve the catalytic efficiency by offering supplementary reactive sites and fostering stronger interactions between the vacancies and the adsorbed AP decomposition products, thus augmenting the overall decomposition mechanism of AP.

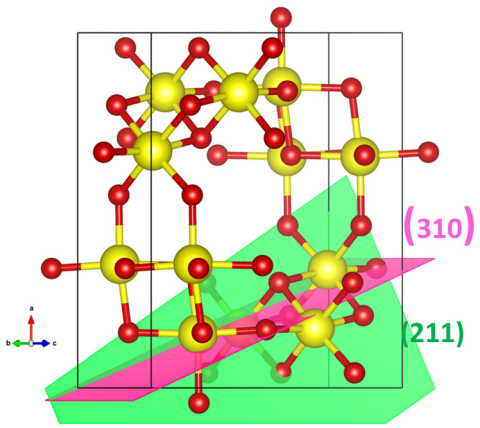

Fig. 8 Crystal structure of α-MnO_2 highlighting the (211) and (310) planes.

Conclusions

The synthesis of α-MnO_2 with two distinct morphologies, nanorods (MnR) and nanocubes (MnC), enabled a systematic investigation into the role of morphology and exposed crystal facets on the thermal decomposition mechanism of AP. A comparative analysis revealed that the MnC, with its smaller particle size, higher specific surface area, and exposure of the high-index (211) facet, significantly lowered the peak decomposition temperature of AP by 111 °C. The surface energies of α-MnO_2 follow the sequence (211) < (310), and oxygen vacancies are easily generated on the (211) surface. Hence, the enhanced formation of oxygen vacancies on the exposed (211) facets of MnC facilitates the generation of abundant Mn^{4+}/Mn^{3+} redox couples which serve as additional reactive sites. These vacancies promote stronger interactions with the intermediates of AP decomposition, thereby accelerating the overall decomposition mechanism and the kinetics. This facet-driven catalytic effect preferentiality promotes one of the competing reactions resulting in the formation of an excess amount of NO_2 during the catalytic reactions. These findings advance the development of tailored α-MnO_2 surface-sensitive nanostructures, where significant improvements in efficiency can be achieved in the fields of catalysis and supercapacitor applications.

Author contributions

The manuscript was written through contributions of all authors. All authors have given approval to the final version of the manuscript.

Conflicts of interest

There are no conflicts to declare.

Data availability

Supplementary information is available. See DOI: **https://doi.org/10.1039/D5CE00732A**.

SEM images,and TEM images, SAED pattern, survey scan XPS spectra, TG-FTIR data of α and β MnO_2 nanorods are supplied as supporting information. Most of the data supporting the findings of this study are included in the article and SI. Additional data are available from the corresponding author upon reasonable request.

Acknowledgements

The authors gratefully acknowledge the support of Mr. Shani Saha and Prof. Neeraj Kumbhakarna from the IC Engine Laboratory, Department of Mechanical Engineering, IIT Bombay, for facilitating the TG-FTIR measurements. Financial support from the Defence Research and Development Organization (DRDO) [Project No. DRDO/ARMREB/HEM/2021/241] and the Faculty Research Grant (FRG), NIT Calicut, is also duly acknowledged. The authors gratefully acknowledge the University of Hyderabad for providing access to the TEM facility, Mr. T. Kasilingam for assistance with image acquisition and IIT Hyderabad for conducting XPS analysis. The authors also acknowledge the Centre for Materials Characterization (CMC), NIT Calicut, for PXRD measurements, and DST-FIST for supporting the FESEM facility at NIT Calicut.

Notes and references

1 M. Liu, L. Piao, L. Zhao, S. Ju, Z. Yan, T. He, C. Zhou and W. Wang, *Chem. Commun.*, 2010, **46**, 1664.
2 S. Hadaoui, G. Tran, A. Naitabdi and A. Courty, *Nanoscale*, 2025, **17**, 3277–3287.
3 D. M. Robinson, Y. B. Go, M. Mui, G. Gardner, Z. Zhang, D. Mastrogiovanni, E. Garfunkel, J. Li, M. Greenblatt and G. C. Dismukes, *J. Am. Chem. Soc.*, 2013, **135**, 3494–3501.
4 S. M. Saju and A. A. Vargeese, *New J. Chem.*, 2024, **48**, 17150–17158.
5 E. Hayashi, Y. Yamaguchi, K. Kamata, N. Tsunoda, Y. Kumagai, F. Oba and M. Hara, *J. Am. Chem. Soc.*, 2019, **141**, 890–900.
6 Y. Kita, M. Kuwabara, K. Kamata and M. Hara, *ACS Catal.*, 2022, **12**, 11767–11775.
7 E. Moharreri, W. A. Hines, S. Biswas, D. M. Perry, J. He, D. Murray-Simmons and S. L. Suib, *Chem. Mater.*, 2018, **30**, 1164–1177.
8 J. Jia, P. Zhang and L. Chen, *Catal. Sci. Technol.*, 2016, **6**, 5841–5847.
9 C. Zhang, F. Ye, S. Tang, Y. Chen and W. Tang, *Inorg. Chem.*, 2025, **64**, 6159–6171.
10 H. Zhao, Y. Dong, P. Jiang, G. Wang, J. Zhang, K. Li and C. Feng, *New J. Chem.*, 2014, **38**, 1743–1750.
11 Y. K. Recepoğlu, N. Kabay, K. Yoshizuka, S. Nishihama, İ. Yılmaz-Ipek, M. Arda and M. Yüksel, *Solvent Extr. Ion Exch.*, 2018, **36**, 499–512.
12 X. Wang, H. Qiu, H. Liu, P. Shi, J. Fan, Y. Min and Q. Xu, *Green Chem.*, 2018, **20**, 4901–4910.
13 N. R. Rondla, J. M. Ogilvie, Z. Pan and C. J. Douglas, *Chem. Commun.*, 2014, **50**, 8974–8977.
14 X. Ma, X. Liu, H. Guo, G. Ren, J. Wen, W. Chen and G. Wang, *Environ. Sci.:Nano*, 2022, **9**, 3780–3788.
15 W. Adamowicz, W. Macyk and M. Kobielusz, *J. Mater. Chem. A*, 2025, **13**, 19623–19630.
16 J. Yan, P. Zhang, D. Chen, J. Cheng, T. Mu, M. Song, S. Li, H. Zhao, G. Chang, R. Lian, C. Liu, W. Huo and D. Kan, *Nanoscale*, 2025, **17**, 9253–9261.
17 J. W. Mullin, Butterworth Heinemann, Crystallization, Oxford, UK, 4th edn, 2001.
18 H.-E. Wang, Z. Lu, D. Qian, S. Fang and J. Zhang, *J. Alloys Compd.*, 2008, **466**, 250–257.
19 C. Liu, S. T. Navale, Z. B. Yang, M. Galluzzi, V. B. Patil, P. J. Cao, R. S. Mane and F. J. Stadler, *J. Alloys Compd.*, 2017, **727**, 362–369.
20 D. Mondal, B. K. Paul, D. Bhattacharya, D. Ghoshal, S. Biswas, K. Das and S. Das, *J. Mater. Chem. C*, 2021, **9**, 5132–5147.
21 G. Wang, B. Tang, L. Zhuo, J. Ge and M. Xue, *Eur. J. Inorg. Chem.*, 2006, **2006**, 2313–2317.
22 Y.-L. Chan, S.-Y. Pung, S. Sreekantan and F.-Y. Yeoh, *J. Exp. Nanosci.*, 2016, **11**, 603–618.
23 G. Cao, L. Su, X. Zhang and H. Li, *Mater. Res. Bull.*, 2010, **45**, 425–428.
24 Y. Xiong, Y. Xie, Z. Li and C. Wu, *Chem. – Eur. J.*, 2003, **9**, 1645–1651.
25 Z.-Y. Yuan, Z. Zhang, G. Du, T.-Z. Ren and B.-L. Su, *Chem. Phys. Lett.*, 2003, **378**, 349–353.
26 M. H. Alfaruqi, J. Gim, S. Kim, J. Song, D. T. Pham, J. Jo, Z. Xiu, V. Mathew and J. Kim, *Electrochem. Commun.*, 2015, **60**, 121–125.
27 A. Xia, W. Yu, J. Yi, G. Tan, H. Ren and C. Liu, *J. Electroanal. Chem.*, 2019, **839**, 25–31.
28 K. Momma and F. Izumi, *J. Appl. Crystallogr.*, 2011, **44**, 1272–1276.
29 T. A. Gokhale, V. V. Phatake and B. M. Bhanage, *Mol. Catal.*, 2022, **533**, 112771.
30 M. R. Shaik, R. Syed, S. F. Adil, M. Kuniyil, M. Khan, M. S. Alqahtani, J. P. Shaik, M. R. H. Siddiqui, A. Al-Warthan, M. A. F. Sharaf, A. Abdelgawad and E. M. Awwad, *Saudi J. Biol. Sci.*, 2021, **28**, 1196–1202.
31 M. Shen, S. J. Zhu, X. Liu, X. Fu, W. C. Huo, X. L. Liu, Y. X. Chen, Q. Y. Shan, H.-C. Yao and Y. X. Zhang, *CrystEngComm*, 2019, **21**, 5322–5331.

32 G. P. Sutton and O. Biblarz, *Rocket Propulsion Elements*, John Wiley & Sons, 2014.
33 A. A. Vargeese, *Combust. Flame*, 2015, **165**, 354–360.
34 V. V. Boldyrev, *Thermochim. Acta*, 2006, **443**, 1–36.
35 S. M. Saju, J. A. Thomas and A. A. Vargeese, *Propellants, Explos., Pyrotech.*, 2025, **50**(4), e12031.
36 A. K. Galwey and P. W. M. Jacobs, *Proc. R. Soc. London, Ser. A*, 1960, **254**, 455–469.
37 L. Mallick, S. Kumar and A. Chowdhury, *Thermochim. Acta*, 2015, **610**, 57–68.
38 Y. L. Zhu, H. Huang, H. Ren and Q. J. Jiao, *J. Energ. Mater.*, 2014, **32**, 16–26.
39 P. Zhou, S. Zhang, Z. Ren, Y. Wang, Y. Zhang and C. Huang, *Inorg. Chem. Front.*, 2022, **9**, 5195–5209.
40 A. G. Keenan and R. F. Siegmund, *Q. Rev., Chem. Soc.*, 1969, 430–452.
41 D. A. Tompsett, S. C. Parker and M. S. Islam, *J. Mater. Chem. A*, 2014, **2**, 15509–15518.
42 L. Li, X. Feng, Y. Nie, S. Chen, F. Shi, K. Xiong, W. Ding, X. Qi, J. Hu, Z. Wei, L.-J. Wan and M. Xia, *ACS Catal.*, 2015, **5**, 4825–4832.